Original Research

In vivo angiogenesis imaging of solid tumors by $\alpha_v\beta_3$-targeted, dual-modality micellar nanoprobes

Chase W Kessinger[1], Chalermchai Khemtong[1], Osamu Togao[2], Masaya Takahashi[2], Baran D Sumer[3] and Jinming Gao[1]

[1]Department of Pharmacology, Harold C Simmons Comprehensive Cancer Center; [2]Advanced Imaging Research Center; [3]Department of Otolaryngology, University of Texas Southwestern Medical Center at Dallas, ND2.210, 5323 Harry Hines Boulevard, Dallas, TX 75390, USA

Corresponding author: Jinming Gao. Email: jinming.gao@utsouthwestern.edu

Abstract

The objective of this study was to develop and evaluate an $\alpha_v\beta_3$-specific nanoprobe consisting of fluorescent superparamagnetic polymeric micelles (FSPPM) for *in vivo* imaging of tumor angiogenesis. Spherical micelles were produced using poly(ethylene glycol)-*b*-poly(D,L-lactide) co-polymers conjugated with tetramethylrhodamine, a fluorescent dye, and loaded with superparamagnetic iron oxide nanoparticles. The resulting micelle diameter was 50–70 nm by dynamic light scattering and transmission electron microscopy measurements. Micelles were encoded with an $\alpha_v\beta_3$-specific peptide, cyclic RGDfK, and optimized for maximum fluorescence and targeting in $\alpha_v\beta_3$-overexpressing cells *in vitro*. In mice, cRGD-FSPPM-treated animals showed $\alpha_v\beta_3$-specific FSPPM accumulation in human lung cancer subcutaneous tumor xenografts. Together with the histological validation, the three-dimensional gradient echo magnetic resonance imaging (MRI) data provide high spatial resolution mapping and quantification of angiogenic vasculature in an animal tumor model using targeted, ultrasensitive MRI nanoprobes.

Keywords: fluorescent polymeric micelles, superparamagnetic iron oxide, cancer molecular imaging, $\alpha_v\beta_3$ integrin, magnetic resonance imaging

Experimental Biology and Medicine 2010; **235**: 957–965. DOI: 10.1258/ebm.2010.010096

Introduction

Angiogenesis plays a critical role in carcinogenesis and cancer metastasis. The formation of new blood vessels from an existing vasculature network is necessary for sustained tumor growth and the exchange of nutrients and metabolic waste. Accurate detection and quantification of tumor angiogenesis is important for early diagnosis of cancer as well as post-therapy assessment of antiangiogenic drugs. Established clinical methods of interrogating tumor angiogenesis rely heavily on the invasive measurement of intratumoral microvascular density (MVD) by the immunohistochemical staining of endothelial markers in biopsied tumor tissue. Although MVD correlations with tumor malignance, stage and invasiveness have been reported, they have shown varying degrees of success in predicting patient response and survival.[1,2] This could be due to the inherent limitation of MVD measurements to follow the dynamic changes in vessel density before, during and after therapeutic interventions. Recently, numerous clinical trials evaluating the utility of antiangiogenic therapies incorporate the use of dynamic contrast enhancement magnetic resonance imaging (DCE-MRI) to non-invasively assess tumor angiogenesis.[3] In DCE-MRI, vascular permeability (e.g. K^{trans}, the transport rate between the vascular and extravascular compartments) of intravenously injected T_1-shortening contrast agents (e.g. Gadoteridol) is analyzed to assess tumor vascularity. Despite the clinical implementation, DCE-MRI is far from precise and specific due to variations in tumor location, size, pathophysiology and the lack of contrast sensitivity.[3] Currently, new imaging methods that allow for highly specific and quantitative detection of angiogenesis-specific biomarkers are under intensive investigation. Novel contrast probes such as small molecular radiotracers, superparamagnetic iron oxide (SPIO) and lipid- and polymer-based nanoparticles are being developed to target different biomarkers of angiogenesis.[4–11] However, current non-invasive methods for visualization and quantification of angiogenic biomarkers have been limited to radiolabeled positron emission tomography (PET) tracers (e.g. vascular endothelial growth

ISSN: 1535-3702

factor and $\alpha_v\beta_3$).[12–14] Despite the high sensitivity of PET, inherent limitations in the spatial resolution (5–10 mm) and high background signals do not allow for three-dimensional (3D) reconstruction and visualization of the angiogenic vasculature.

In this study, we report the development of $\alpha_v\beta_3$-specific, dual-modality, fluorescent superparamagnetic polymeric micelles (cRGD-FSPPM, Scheme 1) for angiogenic imaging of tumors. Integrin $\alpha_v\beta_3$ is a well-established angiogenesis marker that is overexpressed on the surface of neovascular endothelial cells and weakly expressed on non-angiogenic endothelial cells.[15] Specifically, $\alpha_v\beta_3$ integrin expression has been correlated with tumor stage, and the malignant potential of several types of cancer, including lung, breast, colon, and malignant melanoma and squamous cell carcinomas of the skin.[16–18] This nanocomposite probe design exploits the advantages of the MRI ultrasensitivity rendered by the clustered SPIO-loaded micelles, $\alpha_v\beta_3$ specificity by cRGD ligands and target validation by fluorescence functionality. 3D tumor volume images from cRGD-FSPPM nanoprobes illustrate the interconnecting vascular network in A549 lung tumor xenografts *in vivo*. Furthermore, quantitative image analysis demonstrates that this nanoprobe is capable of providing highly specific and quantitative detection of angiogenic 'hot-spots' over the non-targeted, cRAD-FSPPM, control.

Materials and methods

Syntheses and characterization of polyethylene glycol-polylactide co-polymers

Methoxy-polyethylene glycol-polylactide (MeO-PEG-PLA) and maleimide (Mal)-PEG-PLA co-polymers were synthesized by ring-opening polymerization of D,L-lactide using corresponding PEG-OH as macromolecular initiators in refluxing toluene.[19] The polymers were characterized by nuclear magnetic resonance spectroscopy and gel permeation chromatography. PEG-PLA- tetramethylrhodamine (TMR) co-polymer was synthesized by conjugating TMR-5-carbonyl azide (Invitrogen, Carlsbad, CA, USA) to the hydroxyl group of MeO-PEG-PLA in anhydrous toluene at 80°C for four hours.[20] The fluorescent polymer was first dissolved in tetrahydrofuran (THF), filtered and then precipitated from cold hexane and diethyl ether. All resultant polymers had a total molecular weight of 10 kDa with 5 kDa PEG and 5 kDa PLA segments.

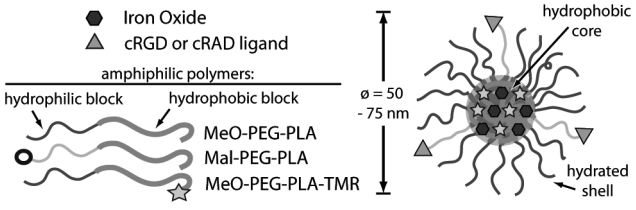

Scheme 1 Fluorescent superparamagnetic polymeric micelle (FSPPM) for molecular imaging of $\alpha_v\beta_3$ integrin expression in angiogenic vasculature of solid tumors

Production of FSPPM

SPIO nanoparticles were synthesized following published methods.[21] The SPIO nanoparticle size distribution was 9 ± 0.9 nm by transmission electron micrographs (TEM) analysis (JEOL 1200 EX at 120 kV). Polymeric micelles were prepared by a solvent evaporation method.[19] Briefly, a mixture of SPIO (4 mg), MeO-PEG-PLA (6 mg), PEG-PLA-TMR (10 mg) and Mal-PEG-PLA (4 mg) in THF (2 mL) was added dropwise to 50 mmol/L 4-(2-hydroxyethyl)-1-piperazineethanesulfonic acid (HEPES) buffer containing 10 mmol/L EDTA (pH 7.4, 18 mL) under sonication. The micelle suspension was then equally divided into two parts, and then shaken on an orbital shaker for four hours to allow THF to evaporate. Each micelle solution was then added a solution of either thiol-terminated cyclic (Arg-Gly-Asp-D-Phe-Lys) (cRGDfK), referred to as cRGD herein or cyclic (Arg-Ala-Asp-D-Phe-Lys) (cRADfK), referred to as cRAD herein (0.4 μmol in 2 mL HEPES buffer). The solutions were then shaken on an orbital shaker overnight for complete conjugations of peptides to maleimide-terminated micelles. Thiol-terminated cRGD and cRAD were obtained by deprotections of thioacetate cRGD and cRAD (Peptides International, Louisville, KY, USA), followed by preparative high performance liquid chromatography (HPLC) purifications. Micelle formulations were filtered through 1.0 μm nylon syringe filters, purified and concentrated using centrifugal filters (100 kDa cutoff, Millipore, Billerica, MA, USA).

Cellular uptake studies

SLK cells, endothelial cells isolated from Kaposi's sarcoma, were incubated for 60 min with micelles and then washed and fixed in 4% paraformaldehyde (pH 7.4), after which they were stained with wheat germ agglutinin (WGA) AlexaFluor488 (W11261; Invitrogen) and mounted with 4′,6-diamidino-2-phenylindole (DAPI) containing media. Micrographs were collected using a Nikon C1 confocal laser scanning microscope and visualized using Nikon C1 free viewer software. For Prussian blue staining, cells were fixed in a 30% acetone and 70% methanol solution. Cells were incubated in a mixture of 10% potassium ferrocyanide and 20% HCl for 30 min, after which the nuclei and cytoplasm were counterstained with Nuclear Fast Red, dehydrated and mounted. For inhibition studies of endocytosis of the FSPPM, SLK cells were preincubated in 400 μM genistein or 20 μg/mL chlorpromazine for 15 min, followed by micelles and inhibitors for 30 min. Cells were then stained with Hoechst 33342 and imaged.

Animal studies

Female athymic nude mice were utilized for this study. All procedures were approved by the Institutional Animal Care and Use Committee at UT Southwestern Medical Center at Dallas and carried out according to its guidelines. All imaging was performed under the inhalational anesthesia isoflurane (1%) mixed with pure oxygen, and administered to a free breathing mouse using a nose cone. Five million

A549 non-small cell lung cancer cells were injected subcutaneously into the left flank of the animal to induce tumor formation. Tumors were randomized into groups ($n = 3$ per group) and imaged at a volume of 300–400 mm^3. FSPPM was administered via tail vein (6 mg Fe/kg) and imaged using a 7 T Varian horizontal bore small animal MRI scanner. T_2^*-weighted (T_2^*-w) images were acquired using a 3D gradient echo sequence (TR = 20 ms; TE = 3 ms; flip angle = 45; NEX = 8; field of view = 30 mm × 30 mm × 15 mm; matrix = 128 × 128 × 64). Images were then processed using ImageJ. 3D models were created using ITK-SNAP software.

Histological analysis

After imaging, the tumor tissue was resected and embedded in optical cutting temperature medium and flash frozen. The tissue was sectioned on a Leica 3050S cryostat at 8 μm and was fixed in −20°C acetone. Immunofluorescence of murine endothelial marker CD31 (platelet/endothelial cell adhesion molecule-1 [PECAM-1]) and $\alpha_v\beta_3$ integrin via CD61 (β_3 integrin) was achieved following standardized protocols using BD Pharmingen primary antibodies 550274 and 550541, respectively. Fluorescently labeled secondary antibodies were obtained from Jackson ImmunoResearch Laboratories, Inc. (West Grove, PA, USA). Stained sections were mounted in a DAPI containing media. Images were collected using a Leica DM5500 microscope with proper excitation and emission filter sets. Prussian blue staining was achieved following the protocol outlined above.

Results

Fluorescence and MR characterization of FSPPM

The FSPPM nanoprobe was produced by encapsulating a cluster of SPIO (diameter: 9 ± 0.9 nm) in the core of PEG-PLA amphiphilic block co-polymer micelles (Scheme 1). To introduce fluorescence functionality, TMR was conjugated to the hydroxyl groups on the hydrophobic PLA segment of the co-polymer (Supplementary information, Figure S1). To optimize the FSPPM formulation for maximum fluorescent output, the weight ratio of PEG-PLA-TMR was varied from 1 to 20 (w/w%) over the non-fluorescent MeO-PEG-PLA co-polymer. Emission spectra showed a maximal fluorescence at 584 nm, consistent with the TMR emission profile. Spectrofluorometric measurements showed relative fluorescence units of 446, 607, 851 and 1212 for 1%, 2%, 5% and 20% at 584 nm, respectively (Figure 1a). Although lower loading percentages had greater fluorescence efficiency on a per dye basis, 20% PEG-PLA-TMR micelles showed the maximum fluorescence output on a per micelle basis and were therefore used for the remainder of the study. For all studies, SPIO was encapsulated in the FSPPM core at 20 wt%. TEM revealed the spherical morphology of the FSPPM nanoprobes with diameters of 57 ± 12 and 53 ± 10 nm for cRGD- and cRAD-FSPPM, respectively (Figure 1b). Negatively stained samples highlighted the core-shell structure of the micelle with a cluster of SPIO loaded in the hydrophobic core (Figure 1b, inset). The hydrodynamic diameters measured by dynamic light scattering were consistent with TEM characterization with diameters of 58.4 ± 9.7 and 55.4 ± 9.8 nm for cRGD- and cRAD-FSPPM, respectively.

The MRI ultrasensitivity of the FSPPM was examined by obtaining the transverse relaxivity of the final formulation. A phantom with varying concentrations of FSPPM solutions was imaged using T_2-weighted spin echo sequences with variable TE times on a 7 T small animal MRI system (Figure S2). The transverse relaxivity of the FSPPM was 406.6 ± 9.1 mmol/L/s Fe at 20°C.

$\alpha_v\beta_3$-targeting specificity of cRGD-FSPPM nanoprobes *in vitro*

The $\alpha_v\beta_3$-targeting specificity and cellular uptake of cRGD-FSPPM was examined in SLK cells, which have been shown to overexpress $\alpha_v\beta_3$ integrin[22] and facilitate $\alpha_v\beta_3$-mediated endocytosis *in vitro*.[23] To verify $\alpha_v\beta_3$ specificity, a non-targeted cRAD-FSPPM control and a competition control of free cRGD peptide co-incubated with cRGD-FSPPM were utilized. cRGD-FSPPM-treated cells showed significantly greater uptake of FSPPM over the non-targeted

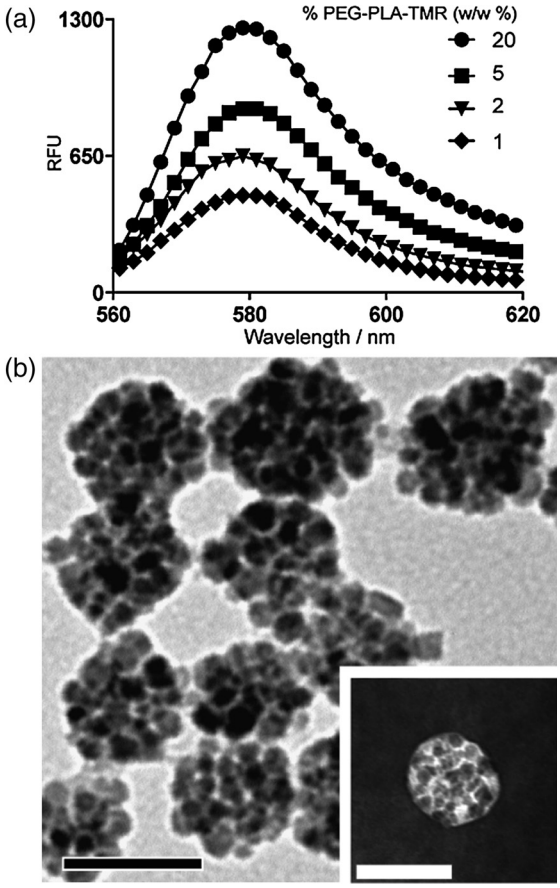

Figure 1 (a) Emission spectra of FSPPM formulations with 1%, 2%, 5% and 20% loading of PEG-PLA-TMR polymer ($\lambda_{ex} = 534$ nm). (b) TEM micrograph of a representative FSPPM sample. The inset shows the same sample stained with 2% phosphotungstic acid. Black punctate structures are the SPIO nanoparticles in the micelle core. Scale bars = 50 nm. FSPPM, fluorescent superparamagnetic polymeric micelle; PEG-PLA-TMR, polyethylene glycol-polylactide-tetramethylrhodamine; TEM, transmission electron microscopy; SPIO, superparamagnetic iron oxide

cRAD-FSPPM control (Figure 2, red fluorescence). Moreover, competitive binding of $\alpha_v\beta_3$ by free cRGD peptide effectively reduced the amount of cRGD-FSPPM uptake to levels equivalent to cRAD-FSPPM-treated cells. Plasma membrane labeling of sialic acid and other saccharides with fluorescently labeled WGA verified the internalization of the FSPPM in cytoplasmic compartments. Prussian blue staining of the cells corroborated the internalized location of the intact FSPPM by staining for the iron in the SPIO (Figure 2). $\alpha_v\beta_3$-targeting specificity and cellular uptake of cRGD-FSPPM were further supported by flow cytometry and the measurement of T_2 relaxation times of treated SLK cells resuspended in agarose gel (Figure S3). Furthermore, inhibitor studies of clathrin and caveolae-mediated endocytosis pathways by chlorpromazine and genistein, respectively, showed that FSPPM nanoprobes were internalized mainly through caveolae-mediated and not clathrin-mediated pathways (Figure S4).

In vivo imaging of $\alpha_v\beta_3$ integrin expression in tumor-bearing mice

In vivo imaging of tumor angiogenesis using cRGD-FSPPM nanoprobes was evaluated in a murine subcutaneous A549 non-small cell lung cancer tumor xenograft model. FSPPM was injected intravenously via the tail vein and imaged using a 3D gradient echo sequence at pre-injection, and 4 and 24 h post-injection of FSPPM. Inspection of the coronal two-dimensional (2D) images collected in the 3D data set showed differences in the distribution pattern and a number of 'hot-spots', hypointense regions-of-interest or darkened areas compared with pre-injection images, in the tumor tissues (red dashed circles) of both cRGD-FSPPM- and cRAD-FSPPM-treated animals (Figure 3a). cRGD-FSPPM-treated tumors showed a connected network of hot-spots in the central and peripheral regions of the tumor, in addition to punctate hot-spots throughout the tumor tissue (Figure 3a, bottom panel, red arrows). In contrast, cRAD-FSPPM-treated tumors showed less hypointense hot-spots, with the majority of them at the skin–tumor interface (Figure 3a, top panel, red arrows). Muscle and fat tissue contrast did not change over the duration of the study. Moreover, in cRGD-FSPPM-treated animals, tumor hot-spot signal intensity was preserved at the 4 and 24 h time points, indicating an internalization or accumulation (no wash-out) of cRGD-FSPPM at those locations.

To validate that the MR hot-spots were a result of FSPPM localization, whole-mount histological sections matching the MR images were stained with Prussian blue. All hot-spot regions on the MR images were matched with the presence of FSPPM (blue precipitate from Prussian blue staining). cRGD-FSPPM-treated animals showed an accumulation of FSPPM associated with the tumor vasculature, while a diffuse staining pattern, likely attributed to the enhanced permeability and retention (EPR) effect, in the cRAD-FSPPM-treated animals was observed at the tumor periphery at the skin–tumor interface (Figure 3b and c). Although Prussian blue staining verifies the presence of iron and therefore SPIO at the location of MRI hot-spots, it cannot provide biological validation of $\alpha_v\beta_3$-expressing endothelial cells. To interrogate the $\alpha_v\beta_3$ targeting at these hot-spots, immunofluorescence images of adjacent tissue sections stained for vascular markers (PECAM-1 or CD31) and $\alpha_v\beta_3$ integrins (CD61) showed cRGD-FSPPM (red fluorescence) to be closely

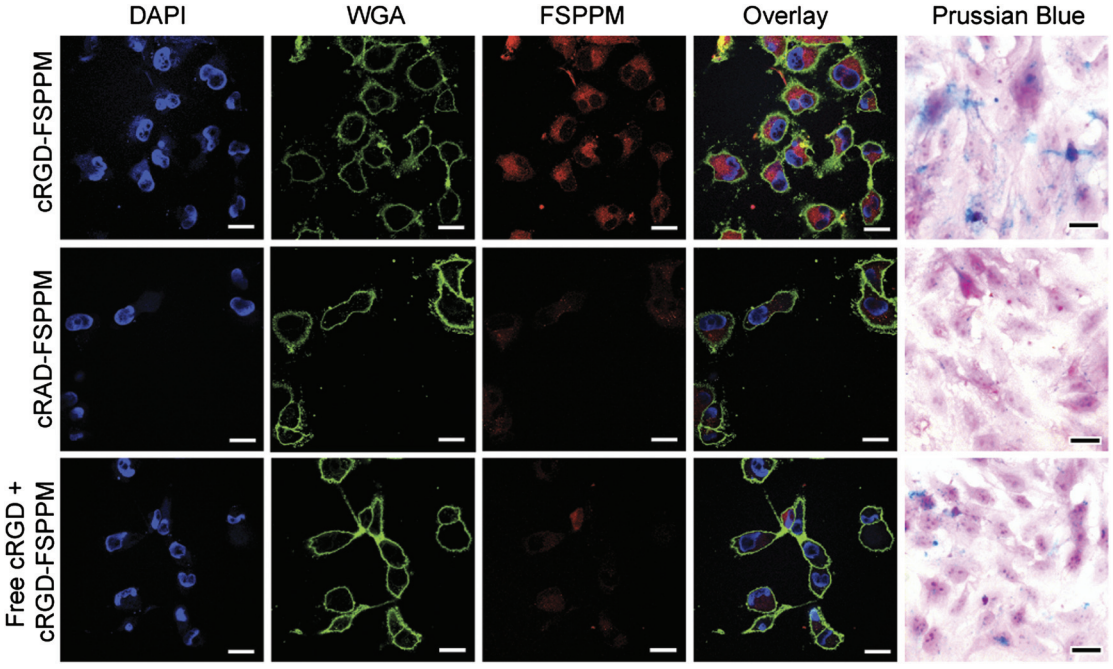

Figure 2 SLK cells were incubated with cRGD-FSPPM, cRAD-FSPPM or free cRGD peptide + cRGD-FSPPM for 30 min. CLSM of cells co-stained with DAPI (blue) and WGA (green) to show the nucleus and plasma membrane, respectively. FSPPM intracellular location (red) was verified by Prussian blue and nuclear fast red staining. Higher uptake of cRGD-FSPPM (red fluorescence and blue granules) compared with other treatment groups is clearly indicated. cRGD, cyclic RGDfK; cRAD, cyclic RADfK; FSPPM, fluorescent superparamagnetic polymeric micelle; CLSM, confocal laser scanning microscopy; DAPI, 4′,6-diamidino-2-phenylindole; WGA, wheat germ agglutinin (A color version of this figure is available in the online journal)

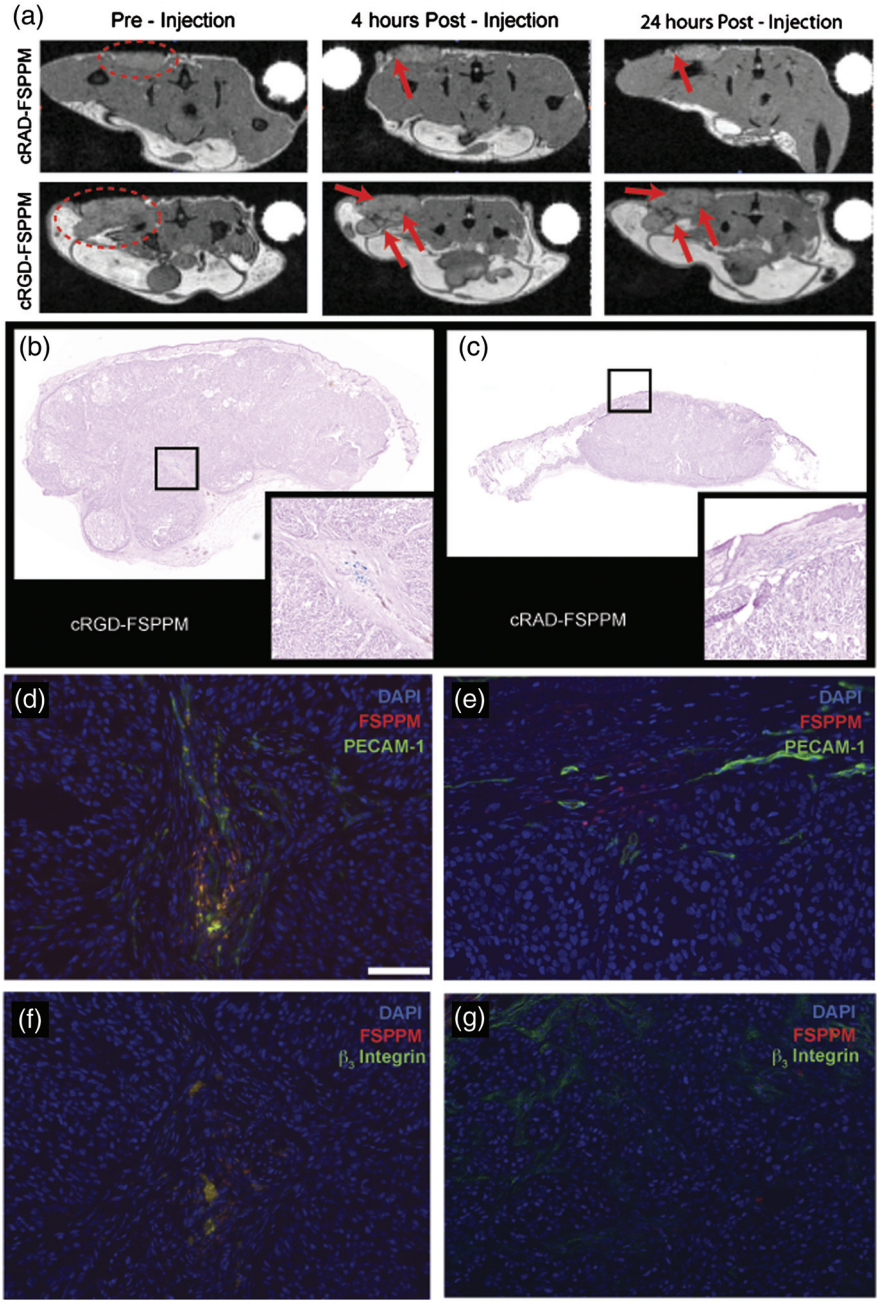

Figure 3 (a) Pre- and post-injection (4 and 24 h) T_2^*-weighted images of A549 tumor-bearing mice injected with cRAD-FSPPM (top) or cRGD-FSPPM (bottom). Dashed circles outline the location of tumor tissues, and red arrows indicate areas of signal intensity loss, compared with pre-injection images. Whole-mount images of Prussian blue staining of analogous tumor tissue sections of cRGD-FSPPM- (b) and cRAD-FSPPM- (c) treated animals show the presence of FSPPM (blue precipitates) in both cases. Inset images are a magnification of hot-spot areas that correlate with hypointense region denoted in (a). Immunofluorescence of adjacent tissue sections stained for PECAM-1 (d, e) and $\alpha_v\beta_3$ via the β_3 integrin (f, g) in cRGD- (d, f) and cRAD-FSPPM- (e, g) treated animals, respectively. FSPPM, fluorescent superparamagnetic polymeric micelle; cRGD, cyclic RGDfK; CRAD, cyclic RADfK; PECAM-1, platelet/endothelial cell adhesion molecule-1 (A color version of this figure is available in the online journal)

associated with the vascular marker, and co-localized with the $\alpha_v\beta_3$ integrin fluorescence (Figure 3d and f). In contrast, cRAD-FSPPM nanoprobes showed little to no co-localization with $\alpha_v\beta_3$ integrins (Figure 3e and g).

Visualization and quantification of tumor angiogenesis

To visualize and quantify the angiogenic regions in the tumor tissue, we constructed 3D volume filled models of the A549 tumor tissue (Figure 4, red volume) and hot-spots (Figure 4, green volume) at an isotropic spatial resolution of 234 μm^3 from the 3D gradient echo data sets. In this analysis, angiogenic hot-spots were identified as voxels whose signal intensity was less than 40% of the tumor parenchyma. This threshold value was determined by the comparison of a histologically confirmed accumulation of FSPPM and a hypointense hot-spot in the tumor tissue of a cRGD-FSPPM-treated animal (Figure 3a and b). All

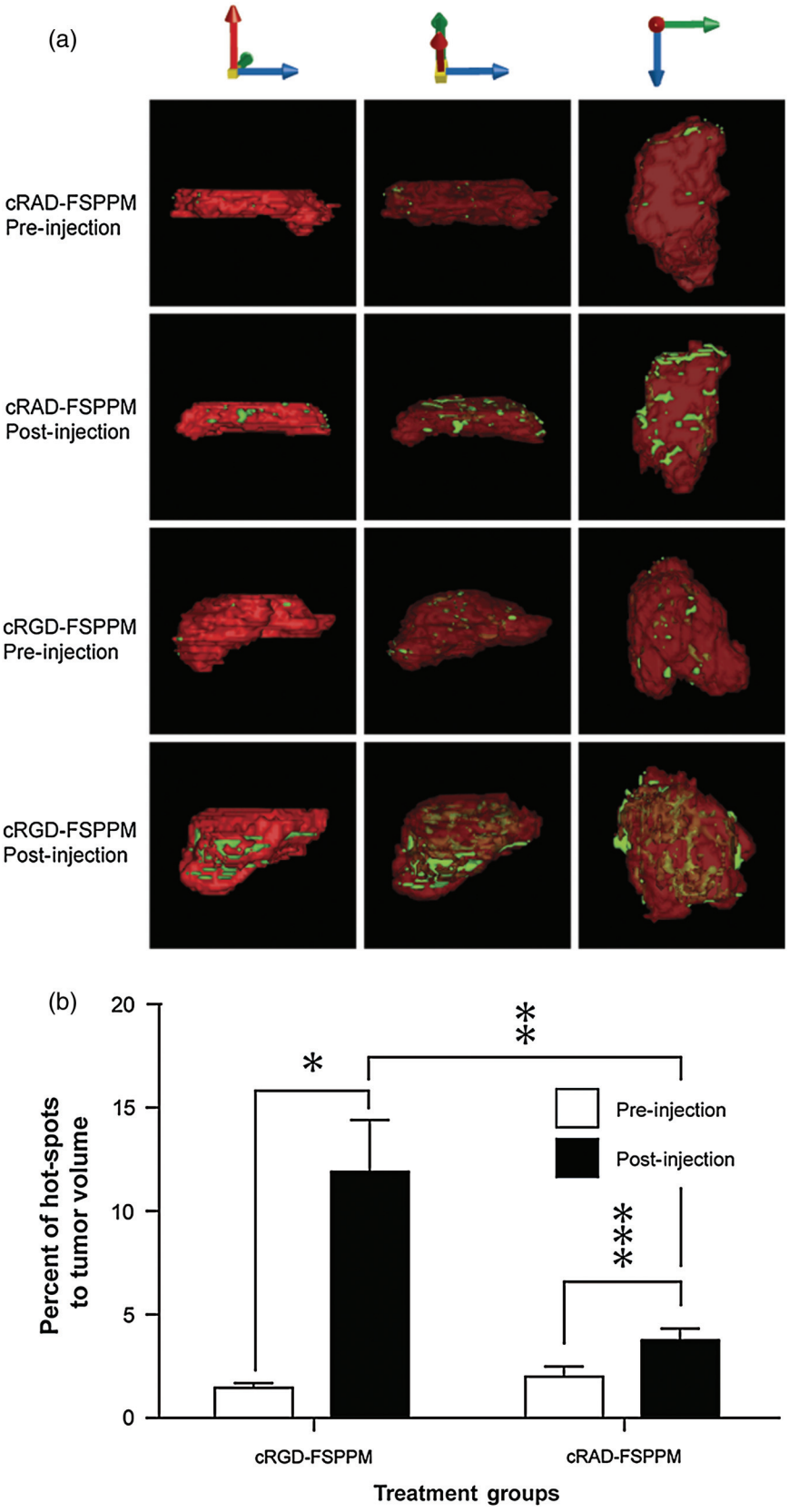

Figure 4 (a) 3D volume renderings of cRAD-FSPPM- and cRGD-FSPPM-treated animals pre- and post-injection. Tumor volumes are shown in red and hot-spots in green. The axis of the volumes was rotated and opacity of the tumor volume was decreased in the middle and right columns to help visualize the interior locations of the hot-spots. (b) Quantification and comparison of 3D volume-based hot-spot density from cRGD-FSPPM and cRAD-FSPPM groups. The *P* values are 0.01 (*), 0.03 (**) and 0.09 (***) from paired groups of comparisons using the Student's *t*-test. 3D, three-dimensional; FSPPM, fluorescent superparamagnetic polymeric micelle; cRAD, cyclic RADfK; cRGD, cyclic RGDfK (A color version of this figure is available in the online journal)

hot-spots were located within the tumor boundaries. It is important to note that choosing the threshold value from a non-confirmed location in the tumor may lead to fluctuation in the angiogenic quantification. Multiple angles and varied opacities of the tumor volumes allows for the spatial localization of the hot-spot areas. In the precontrast images, sporadic hot-spot patterns were observed mostly on the surface of the solid tumors in both animals, which can be caused by magnetic susceptibility changes at the tissue/air or tumor tissue/fat tissue interfaces (Figure 4a). In the post-contrast images (4 h after injection), cRGD-FSPPM-treated tumors showed an extensive connected branching architecture of hot-spots throughout the tumor volume. In contrast, cRAD-FSPPM-treated tumors showed that the majority of the hot-spots were located in the highly perfused regions at the skin–tumor interface. Importantly, those punctate hot-spots in the 2D images can now be visualized as a continuation of an angiogenic hot-spot network. Furthermore, the volume-based tumor hot-spot density can be measured and compared pre- and post-injection to quantify the amount of angiogenesis in the tumor tissue (Figure 4b, $n = 3$ for each group). In pre-injection images, the percentage of hot-spot pixels to tumor volume pixels was $1.8 \pm 1.0\%$ and $1.4 \pm 0.4\%$ for cRAD-FSPPM and cRGD-FSPPM-treated animals, respectively (Figure 4b, white boxes). In post-injection images, the amount of hot-spots increased to $3.7 \pm 1.0\%$ and $11.8 \pm 4.3\%$ in cRAD- and cRGD-FSPPM groups, respectively. Statistically significant differences (Student's *t*-test, $^{**}P$ value $= 0.03$) in post-injection percentage between cRGD- and cRAD-FSPPM demonstrate the targeting and accumulation of cRGD-FSPPM in the areas of angiogenesis (Figure 4b, black boxes) over cRAD-FSPPM. Comparison of the pre- and post-injection percentages also showed a significant difference in the cRGD-FSPPM group ($^{*}P$ value $= 0.01$) and no difference in the cRAD-FSPPM group ($^{***}P$ value $= 0.09$).

Discussion

In this study, cRGD-FSPPM nanoprobes were developed and their ability to bind specifically to $\alpha_v\beta_3$ integrin expressing endothelial cells *in vitro* and *in vivo* was investigated using MRI and fluorescence imaging techniques. Moreover, 3D reconstruction of the T_2^*-w MRI data sets allowed for the non-invasive visualization and quantification of angiogenic tumor vascular networks at an isotropic resolution of 234 μm^3.[12–14] Recently, Lanza and co-workers reported the ability to reconstruct 3D T_1-weighted MRI data sets, with non-isotropic volumes greater than 390 μm^3, to visualize angiogenic vasculature using Gd-DOTA (~130,000 ions/particle)-loaded perfluorcarbon emulsion nanoparticles targeted to both $\alpha_v\beta_3$ and $\alpha_v\beta_5$ integrins.[24] In this study, the ultrasensitive detection of superparamagnetic nanoparticles by the T_2^*-w method allows for detailed visualization and accurate 3D mapping of angiogenic vasculatures in the tumor tissue.

The use of polymer- and lipid-based platforms as nanocarriers of imaging agents has proven to be beneficial in increasing imaging sensitivity,[11,25] prolonging blood circulation half-times,[26] passive targeting of tumor tissues via the EPR effect[27,28] and the active targeting of cancer markers such as Her2-Neu,[5] folate,[6] transferrin receptors[7] and $\alpha_v\beta_3$ integrin.[4,8–11] Although multiple imaging platforms have shown targeting efficacy *in vitro* and *in vivo*, it is only recently that these formulations have been adapted or combined for multimodality imaging applications. Recently, Sailor and co-workers have introduced SPIO and quantum dots (QDs) in the micellar systems to generate a dual-modality nanoprobe.[29] In our study, we chose to use a small hydrophobic molecular dye to maximize the payload of SPIO to increase MRI sensitivity of the FSPPM while avoiding possible cellular toxicity from QDs. Our FSPPM platform had several potential advantages compared with current molecular imaging agents. First, the clustering of uniform SPIO in the core of micelles has demonstrated MRI ultrasensitivity with detection limits in the nanomolar and picomolar concentration using conventional T_2-weighted and off-resonance saturation MR imaging sequences, respectively.[11,25,30] Conventional T_1-weighted contrast agents (e.g. Gd-DTPA) have detection limits in the millimolar to micromolar range.[31] Moreover, the FSPPM showed a 4.5-fold greater transverse relaxivity on a per iron atom basis than Feridex,[32] a clinically approved SPIO formulation. Second, the cRGD-FSPPM benefits from improved specificity for angiogenic vessels in the tumor tissue due to its active targeting to $\alpha_v\beta_3$ integrin via the cRGD ligands. Third, the incorporation of a fluorescent moiety allowed for the validation of FSPPM targeting *in vitro* and *in vivo*, using fluorescence imaging techniques. Previous polymer- and lipid-based nanoprobes have also shown targeting via immunofluorescence analysis, but have used externally displayed fluorophores.[4,8] In our nanocomposite design, the TMR dye is protected from inadvertent cleavage and protein interactions by its encapsulation in the core of the FSPPM. This characteristic could allow for the prolonged fluorescence output needed for other *in vivo* fluorescence imaging studies. Moreover, incorporation of hydrophobic near-infrared fluorescent dyes could also allow for deeper tissue imaging using other non-invasive optical methods.

Specific targeting to $\alpha_v\beta_3$ integrins and subsequent receptor-mediated endocytosis of cRGD-FSPPM was demonstrated in SLK cells relative to studies of cRAD-FSPPM and the addition of free cRGD peptides to cRGD-FSPPM controls using both MR and fluorescence imaging techniques. In tumor-bearing mice, differences in the intratumoral distribution of the targeted and non-targeted FSPPM were also compared. Most of cRGD-FSPPM was localized to vascular areas throughout the tumor volume and cRAD-FSPPM was found only at the tumor periphery. One of the limitations in displaying the angiogenic hot-spots in 2D slices is the lack of spatial context to appreciate the network structures of the tumor vasculature, which makes it difficult for the accurate quantification of tumor angiogenesis in the whole tumor volume. To overcome this limitation, isotropic 3D data were gathered to construct the volume filled models of the A549 tumors where an interconnecting vasculature network was demonstrated by cRGD-FSPPM nanoprobes. This $\alpha_v\beta_3$-targeted

nanoprobe was further able to quantify the extent of tumor angiogenesis by comparing the pre- and post-injection images over the cRAD-FSPPM control.

In summary, this paper describes the development and application of dual-modality nanoprobes for angiogenesis imaging of solid tumors. The combination of molecular targeting to an angiogenic biomarker (i.e. $\alpha_v\beta_3$) and the dual-modality imaging design allowed for an accurate and quantitative characterization of tumor angiogenesis. This new paradigm offers exciting opportunities for early detection of solid tumors and non-invasive post-therapy assessment of antiangiogenic drugs.

Author contributions: All authors contributed to the result interpretation and review of the manuscript. CWK conducted the experiments, collection and analysis of the data; CK assisted in the synthesis and fabrication of FSPPM; OT and MT aided in the collection and analysis of MRI images; CWK and JG designed the experiments and wrote the manuscript; and BDS contributed to manuscript preparation.

ACKNOWLEDGEMENTS

We thank the National Institutes of Health (EB005394 and CA129011) for grant support to JG. CK was supported by a DOD Breast Cancer Research Program Multidisciplinary Postdoctoral Fellowship (W81XWH-06-1-07751). This is CSCN000 from the Programs in Cell Stress and Cancer Nanomedicine, Harold C Simmons Comprehensive Cancer Center, UT Southwestern Medical Center at Dallas.

REFERENCES

1 Chandrachud LM, Pendleton N, Chisholm DM, Horan MA, Schor AM. Relationship between vascularity, age and survival in non-small-cell lung cancer. *Br J Cancer* 1997;**76**:1367–75
2 Weidner N, Semple JP, Welch WR, Folkman J. Tumor angiogenesis and metastasis – correlation in invasive breast carcinoma. *N Engl J Med* 1991;**324**:1–8
3 O'Connor JP, Jackson A, Parker GJ, Jayson GC. DCE-MRI biomarkers in the clinical evaluation of antiangiogenic and vascular disrupting agents. *Br J Cancer* 2007;**96**:189–95
4 Mulder WJ, Strijkers GJ, Habets JW, Bleeker EJ, van der Schaft DW, Storm G, Koning GA, Griffioen AW, Nicolay K. MR molecular imaging and fluorescence microscopy for identification of activated tumor endothelium using a bimodal lipidic nanoparticle. *FASEB J* 2005;**19**:2008–10
5 Artemov D, Mori N, Okollie B, Bhujwalla ZM. MR molecular imaging of the Her-2/neu receptor in breast cancer cells using targeted iron oxide nanoparticles. *Magn Reson Med* 2003;**49**:403–8
6 Sonvico F, Mornet S, Vasseur S, Dubernet C, Jaillard D, Degrouard J, Hoebeke J, Duguet E, Colombo P, Couvreur P. Folate-conjugated iron oxide nanoparticles for solid tumor targeting as potential specific magnetic hyperthermia mediators: synthesis, physicochemical characterization, and *in vitro* experiments. *Bioconjug Chem* 2005;**16**:1181–8
7 Hogemann-Savellano D, Bos E, Blondet C, Sato F, Abe T, Josephson L, Weissleder R, Gaudet J, Sgroi D, Peters PJ, Basilion JP. The transferrin receptor: a potential molecular imaging marker for human cancer. *Neoplasia* 2003;**5**:495–506
8 Koole R, van Schooneveld MM, Hilhorst J, Castermans K, Cormode DP, Strijkers GJ, de Mello Donega C, Vanmaekelbergh D, Griffioen AW, Nicolay K, Fayad ZA, Meijerink A, Mulder WJ. Paramagnetic lipid-coated silica nanoparticles with a fluorescent quantum dot core: a new contrast agent platform for multimodality imaging. *Bioconjug Chem* 2008;**19**:2471–9
9 Zhang C, Jugold M, Woenne EC, Lammers T, Morgenstern B, Mueller MM, Zentgraf H, Bock M, Eisenhut M, Semmler W, Kiessling F. Specific targeting of tumor angiogenesis by RGD-conjugated ultrasmall superparamagnetic iron oxide particles using a clinical 1.5-T magnetic resonance scanner. *Cancer Res* 2007;**67**:1555–62
10 Cai W, Chen X. Multimodality molecular imaging of tumor angiogenesis. *J Nucl Med* 2008;**49**(Suppl. 2):113S–28S
11 Khemtong C, Kessinger CW, Ren J, Bey EA, Yang SG, Guthi JS, Boothman DA, Sherry AD, Gao J. *In vivo* off-resonance saturation magnetic resonance imaging of alphavbeta3-targeted superparamagnetic nanoparticles. *Cancer Res* 2009;**69**:1651–8
12 Cai W, Chen K, Mohamedali KA, Cao Q, Gambhir SS, Rosenblum MG, Chen X. PET of vascular endothelial growth factor receptor expression. *J Nucl Med* 2006;**47**:2048–56
13 Zhang X, Xiong Z, Wu Y, Cai W, Tseng JR, Gambhir SS, Chen X. Quantitative PET imaging of tumor integrin alphavbeta3 expression with 18F-FRGD2. *J Nucl Med* 2006;**47**:113–21
14 Chen X, Hou Y, Tohme M, Park R, Khankaldyyan V, Gonzales-Gomez I, Bading JR, Laug WE, Conti PS. Pegylated Arg-Gly-Asp peptide: 64Cu labeling and PET imaging of brain tumor alphavbeta3-integrin expression. *J Nucl Med* 2004;**45**:1776–83
15 Brooks PC, Clark RA, Cheresh DA. Requirement of vascular integrin alpha v beta 3 for angiogenesis. *Science* 1994;**264**:569–71
16 Horak ER, Leek R, Klenk N, LeJeune S, Smith K, Stuart N, Greenall M, Stepniewska K, Harris AL. Angiogenesis, assessed by platelet/endothelial cell adhesion molecule antibodies, as indicator of node metastases and survival in breast cancer. *Lancet* 1992;**340**:1120–4
17 Meitar D, Crawford SE, Rademaker AW, Cohn SL. Tumor angiogenesis correlates with metastatic disease, N-myc amplification, and poor outcome in human neuroblastoma. *J Clin Oncol* 1996;**14**:405–14
18 Vosseler S, Mirancea N, Bohlen P, Mueller MM, Fusenig NE. Angiogenesis inhibition by vascular endothelial growth factor receptor-2 blockade reduces stromal matrix metalloproteinase expression, normalizes stromal tissue, and reverts epithelial tumor phenotype in surface heterotransplants. *Cancer Res* 2005;**65**:1294–305
19 Nasongkla N, Bey E, Ren J, Ai H, Khemtong C, Guthi JS, Chin SF, Sherry AD, Boothman DA, Gao J. Multifunctional polymeric micelles as cancer-targeted, MRI-ultrasensitive drug delivery systems. *Nano Lett* 2006;**6**:2427–30
20 Luo L, Tam J, Maysinger D, Eisenberg A. Cellular internalization of poly(ethylene oxide)-*b*-poly(epsilon-caprolactone) diblock copolymer micelles. *Bioconjug Chem* 2002;**13**:1259–65
21 Sun S, Zeng H. Size-controlled synthesis of magnetite nanoparticles. *J Am Chem Soc* 2002;**124**:8204–5
22 Rader C, Popkov M, Neves JA, Barbas CF. Integrin alpha v beta 3-targeted therapy for Kaposi's sarcoma with an *in vitro*-evolved antibody. *FASEB J* 2002;**16**:2000–2
23 Nasongkla N, Shuai X, Ai H, Weinberg BD, Pink J, Boothman DA, Gao J. cRGD-functionalized polymer micelles for targeted doxorubicin delivery. *Angew Chem Int Ed Engl* 2004;**43**:6323–7
24 Schmieder AH, Caruthers SD, Zhang H, Williams TA, Robertson JD, Wickline SA, Lanza GM. Three-dimensional MR mapping of angiogenesis with alpha5beta1(alpha nu beta3)-targeted theranostic nanoparticles in the MDA-MB-435 xenograft mouse model. *FASEB J* 2008;**22**:4179–89
25 Ai H, Flask C, Weinberg B, Shuai X, Pagel MD, Farrell D, Duerk J, Gao JM. Magnetite-loaded polymeric micelles as ultrasensitive magnetic-resonance probes. *Adv Mater* 2005;**17**:1949–52
26 Moghimi SM, Hunter AC, Murray JC. Long-circulating and target-specific nanoparticles: theory to practice. *Pharmacol Rev* 2001;**53**:283–318
27 Hashizume H, Baluk P, Morikawa S, McLean JW, Thurston G, Roberge S, Jain RK, McDonald DM. Openings between defective endothelial cells explain tumor vessel leakiness. *Am J Pathol* 2000;**156**:1363–80
28 Maeda H. The enhanced permeability and retention (EPR) effect in tumor vasculature: the keyb role of tumor-selective macromolecular drug targeting. *Adv Enzyme Regul* 2001;**41**:189–207
29 Park JH, von Maltzahn G, Ruoslahti E, Bhatia SN, Sailor MJ. Micellar hybrid nanoparticles for simultaneous magnetofluorescent imaging and drug delivery. *Angew Chem Int Ed Engl* 2008;**47**:7284–8

30 Mills PH, Ahrens ET. Theoretical MRI contrast model for exogenous T2 agents. *Magn Reson Med* 2007;**57**:442–7
31 Ahrens ET, Rothbacher U, Jacobs RE, Fraser SE. A model for MRI contrast enhancement using T1 agents. *Proc Natl Acad Sci USA* 1998;**95**:8443–8
32 Barcena C, Sra AK, Chaubey GS, Khemtong C, Liu JP, Gao J. Zinc ferrite nanoparticles as MRI contrast agents. *Chem Commun (Camb)* 2008;**19**:2224–6

(Received March 13, 2010, Accepted May 7, 2010)